# Detection of human influences on temperature seasonality from the 19th century

Jianping Duan[1★], Zhuguo Ma[1], Peili Wu[2], Elena Xoplaki[3], Gabriele Hegerl[4], Lun Li[5], Andrew Schurer[4], Dabo Guan[6,7], Liang Chen[1], Yawen Duan[1] & Jürg Luterbacher[3,8]

[1]Key Laboratory of Regional Climate-Environment for Temperate East Asia, Institute of Atmospheric Physics, Chinese Academy of Sciences, 100029 Beijing, China. [2]Met Office Hadley Centre, Exeter EX1 3PB, UK. [3]Department of Geography, Justus Liebig University of Giessen, 35390 Giessen, Germany. [4]School of GeoSciences, University of Edinburgh, Crew Building, Alexander Crum Brown Road, Edinburgh EH9 3FF, UK. [5]Chinese Academy of Meteorological Sciences, 100081 Beijing, China. [6]Water Security Research Centre, Tyndall Centre for Climate Change Research, School of International Development, University of East Anglia, Norwich NR4 7TJ, UK. [7]Department of Earth System Sciences, Tsinghua University, Beijing 100080, China. [8]Centre of International Development and Environmental Research, Justus Liebig University of Giessen, 35390 Giessen, Germany.

★e-mail: duanjp@tea.ac.cn

It has been widely reported that anthropogenic warming is detectable with high confidence after the 1950s. However, current palaeoclimate records suggest an earlier onset of industrial-era warming. Here, we combine observational data, multi-proxy palaeo records and climate model simulations for a formal detection and attribution study. Instead of the traditional approach to the annual mean temperature change, we focus on changes in temperature seasonality (i.e., the summer-minus-winter temperature difference) from the regional to whole Northern Hemisphere scales. We show that the detectable weakening of temperature seasonality, which started synchronously over the northern mid-high latitudes since the late 19th century, can be attributed to anthropogenic forcing. Increased greenhouse gas concentrations are the main contributors over northern high-latitudes, while sulphate aerosols are the major contributors over northern mid-latitudes. A reduction in greenhouse gas emissions and air pollution is expected to mitigate the weakening of temperature seasonality and its potential ecological effects.

It is now common knowledge that human activities have a profound influence on the Earth's climate[1]; the most evident influence is the trend of continuing warming in the surface air temperature and the increased occurrence of climate extremes since the 1950s[1-3]. In addition to changes in the mean and extremes, the warming climate will, as a consequence, affect organisms and ecological systems, such as species physiology[4], ecological stability[5] and ecological functions[6]. One of the primary drivers of these ecological effects is the change in the magnitude of the annual temperature cycle (ATC), which is calculated as the summer-minus-winter temperature difference[7-8]. Emerging evidence has shown prominent ATC weakening in the northern mid-high latitudes during the past several decades[8-10]. Extensions in the growing season[11] and spatial and temporal adaptations of several plants[12] have occurred either regionally or globally as a consequence of the weakened ATC. Based on climate model simulations, the recent weakening of temperature seasonality has been attributed to anthropogenic forcing[13].

It has long been suspected that the human influence on the climate may have started much earlier than that in the recent data-rich period[14]. Because of the limitations of early instrumental observations and temporal variations in the strength of anthropogenic influence combined with internal climate variability and changes in natural external forcing factors, the detection and attribution of human influences on earlier climate changes have always been difficult to perform. Based on palaeoclimate records, a recent study reported that the onset of industrial-era warming across the oceans and continents occurred earlier than the 20th century, suggesting that the greenhouse forcing of industrial-era warming commenced as early as the mid-nineteenth century[15]. Moreover, a tree-ring-based study from the Tibetan Plateau (TP) extended the records of the magnitude of the ATC back to the year 1700[16]; this extended record shows that the onset of weakening temperature seasonality may have occurred as early as the 1870s, coinciding with an increase in human-induced atmospheric sulphate concentrations recorded in an ice core from the Dasuopu glacier (28°23'N, 85°43'E; 7200 m asl)[17]. However, as shown in Fig. 1, both the seasonal warming rates and the trends in the magnitude of the ATC show strong spatial variability. Therefore, it is important to explore the detectability of earlier human influences on temperature change, as broadly as historical records allow, to determine whether these recent findings bear any global implications.

Here, we examine changes in the magnitude of the ATC based on available proxy records and instrumental observations in four regions that show prominent weakening in the magnitude of the ATC (marked by the boxes shown in Fig. 1), as well as in the northern mid-high latitudes. Well-validated proxy data from Europe (1500-2004)[18] and the TP (1700-2011)[16] are used to explore the changes in the magnitude of the ATC from the pre- to post-industrial period; then, the CRU4.6 land surface air temperature since 1850[19] is used to examine broader spatial patterns (Methods). Historical ensemble simulations from the fifth Coupled Model Intercomparsion Project (CMIP5) driven by all forcings and separate external forcings[20] are used for detection and attribution (D&A hereafter).

**Changes in the trend of the magnitude of the ATC**

A change-point analysis shows that the sustained and significant weakening in the magnitude of the ATC in Europe started in 1865 (Fig. 2a). Based on a 312-year reconstruction of the magnitude of the ATC[16], the change-point analysis reveals that the TP has experienced persistent and significant ATC weakening since 1872, while a weak and insignificant strengthening occurred during 1700-1873 (Fig. 2b). There is no ATC proxy evidence available that is long enough to identify when the sustained and significant ATC weakening started in northeastern Asia (NEA), North America (NA), the northern mid-latitudes (NHM), the northern high-latitudes (NHH) and the northern mid-high-latitudes (NH). However, observations starting in 1851 show discernible weakening in the magnitude of the ATC in all of these regions (Fig. 2c-g). These results indicate that although the specific year when the magnitude of the ATC began weakening might not be identical among all regions, prominent ATC weakening has occurred widely since the late 19th century.

## Changes in the magnitude of the ATC related to different forcings

Climate model simulations driven by all historical forcings (i.e., natural and anthropogenic, ALL) can generally reproduce the observed changes in temperature seasonality since 1851 (Fig. 1). However, the simulated trends in the magnitude of the ATC driven by separate forcings appear to be different (Fig. 3). The spatial patterns of the trends in the magnitude of the ATC in the ALL simulations and the anthropogenic forcing only simulations (ANT) are very similar and both are consistent with the observations. Both the spatial pattern and the significant regions of the weakening in the magnitude of the ATC are different from those of indicated by the observations when only natural forcings (NAT) are applied. Interestingly, greenhouse gas (GHG)-induced ATC weakening mainly occurs in the northern high latitudes (north of 60°N), while the anthropogenic aerosol (AA)-triggered ATC weakening occurs in the northern mid-latitudes (30-60°N).

Thus, there are two critical anthropogenic factors that contribute to the weakening in the magnitudes of the ATC: GHG concentrations and AA loadings (Supplementary Figure 1). Due to their different radiative properties, GHGs and AAs have different effects on the local ATC. Increased GHG concentrations reduce outgoing long wave radiation from the surface and prevent the surface temperature from falling. This pattern is most effective over the high-altitude[21] and high-latitude regions[22,23] in winter. AAs dominated by sulphate aerosols[24,25], on the other hand, act to reflect/scatter incoming solar radiation and prevent the surface temperature from rising. This pattern is, therefore, most effective over the subtropical/mid-latitude regions, which have the largest AA loadings[26] during the summer when sunlight is the strongest. In addition to their direct effect, the indirect effect of aerosols on clouds amplifies their influence on short wave scattering, causing net cooling, which is most effective in summer[27].

As shown in Fig. 2, the temporal evolution of the magnitude of the ATC approximately follows those of the GHG emissions[28] and the sulphate aerosol concentration levels recorded in Greenland ice cores over the past half millennium[29] (i.e., a small change preceding the 1860s with a prominent increase thereafter resulting from human emissions) (Fig. 2a). This consistency indicates a potential linkage between human emissions and the weakened ATC. Moreover, a millennial record of atmospheric sulphate concentrations from a TP ice core confirms that human-induced atmospheric sulphate concentrations increase after 1870[17] (Fig. 2b).

**Detection and attribution analysis of the change in the magnitude of the ATC**

Further D&A analyses based on simulations derived from 45 Earth system models (Methods) are utilized to distinguish anthropogenic signals from natural forcing over different spatial regions (Fig. 4). The D&A analysis period is 1872-2001 for the TP and 1865-2004 for the other six regions (for details on the analysis period selection, please see the Methods). Based on one-, two- and three-signal D&A analyses, scaling factors and their 90% confidence intervals are obtained for different forcings in all regions. In all cases, the residual consistency test (RCT) does not indicate inconsistency between the regression residuals and the model-simulated variability (i.e., RCT > 0.1 in all cases). Detection is confirmed if the 90% confidence interval of the scaling factor is above zero, and attribution is claimed by the analysis if this confidence interval also includes one. The one-signal D&A analysis shows that the ALL and ANT response patterns are fully detectable in the analysed regions, except for the high northern latitudes (Fig. 4a). Conversely, NAT forcing is detectable only at high northern latitudes. The failed detection of the ALL and ANT forcings in the high northern latitudes may be related to the scarce observation data available representing large spatial scales (Supplementary Figure 2) and, thus, a large amount of noise was produced. The ALL forcing is attributable in Europe and North America, while the ANT forcing is attributable in Europe, the TP, North America, and the northern mid-high-latitudes. However, the model simulations underestimate both the ALL and ANT responses in northeastern Asia and the northern mid-latitudes. These underestimations are also present in the linear trends in the magnitude of the ATC between the observations and simulations (Fig. 1e, f); the observations show the greatest weakening in the magnitude of the ATC in the NEA (Supplementary Figure 3). An additional two-signal D&A analysis shows that ANT can be distinguished successfully from NAT in six out of seven regions but fails over the high northern latitudes. This is consistent with the results from the one-signal D&A analysis. There is also a generally better agreement between the simulated and observed magnitude of the ATC in the other six regions, compared to that over the high northern latitudes, although there is a tendency for the simulated magnitude of the ATC to be smaller than the observed trends (Supplementary Figure 4). Based on the results presented in Fig. 3, the three-signal D&A analysis (i.e., GHG, NAT and AA) is used to examine whether the latitude-dependent forcings of GHGs or AAs on the weakened magnitude of the ATC can be detected and distinguished from the other two forcings. The results show that the AA forcing can be distinguished from the GHG and the NAT forcings over the northern mid-latitudes, but the GHG forcing cannot be distinguished from the AA and NAT forcings over the high northern latitudes. Consistent with the results presented in Fig. 3, the weakening of the ATC in the northern mid-latitudes can be attributed to AAs, which are dominated by sulphate aerosols, but not to GHGs and NAT. Specifically, GHG and NAT forcings present an obvious underestimation; the underestimation derived from the NAT forcing is much more greater than that derived from the GHG forcing (the scaling factors of GHGs and NAT are approximately 5 and 10, respectively). For the northern mid-high-latitudes, although AAs, GHGs and NAT are detected in the weakened ATC, AAs and GHGs more attributable than NAT (i.e., the scaling factors of GHGs and AAs are closer 1 than that of NAT). These results indicate that AAs are the most important factor for northern mid-latitude ATC weakening, while AAs and GHGs show a greater possibility of contributing to ATC weakening in the northern mid-high-latitudes. All of the D&A analyses fail over the high northern latitudes, possibly due to the small amount of data available to represent large spatial scales (Supplementary Figure 2).

In conclusion, our study indicates that the regime shift in temperature seasonality in approximately the 1870s identified over the TP also occurred in Europe, indicating a broad weakening of the magnitude of the ATC since the late 19$^{th}$ century. Although different magnitudes of weakening in the temperature seasonality exist between regions, the D&A analyses demonstrate that anthropogenic signals are detectable in the long-term, with a widespread weakening of temperature seasonality since the late 19th century. In addition to the increased concentrations of GHGs and atmospheric sulphate loadings, which are identified as critical contributors to long-term temperature seasonality weakening, latitude-dependent effects of these two factors on temperature seasonality are found; GHGs are mainly responsible for the weakening in the temperature seasonality in the northern high latitudes, while AAs are the key cause of weakening in the northern mid-latitudes. These results imply that a policy of reducing greenhouse gas emissions and air pollution can mitigate the anthropogenic weakening of the temperature seasonality.

## Methods

**Climatic and environmental data.** Summer and winter temperatures are defined as the mean temperature of June-August and the mean temperature of the previous December-February, respectively. The amplitude of the ATC is calculated as the difference between the summer temperature and the winter temperature. Gridded data of CRUTEM4.6 land surface air temperature at a spatial resolution of 5° by 5° starting in 1850[19] (https://www.metoffice.gov.uk/hadobs/crutem4/data/download.html) were used to show the trends in the seasonal warming rates and the magnitude of the ATC at a global scale (Fig. 1) and the D&A analyses in the five regions (Supplementary Table 2). The reconstructed magnitude of the ATC for Europe (EU) is the reconstructed summer temperature minus the reconstructed winter temperature derived from reference 18, which covers the period 1500-2004 and has a high consistency with the regionally averaged magnitude of the ATC obtained from the CRUTEM4.6 grid data ($r_{1851\text{-}2004}$ = 0.92) (Supplementary Figure 5). The ATC proxy series for the TP is derived from reference 16 and covers the period 1700-2011. Although the ATC proxy series from the TP was used to reflect the temperature difference in the mean temperature of July-September minus that of the previous November-February in the original study[16], it is also a good proxy for the temperature difference between the mean temperature of June-August and that of the previous December-February, as the two seasonal temperature difference series are almost identical ($r_{1952\text{-}2013}$ = 0.84) (Supplementary Figure 6). Additional comparisons between the magnitude of the ATC proxy series from the TP and the observed magnitude of the ATC series from northeastern India (http://www.tropmet.res.in/static_page.php?page_id=54) in the common period 1902-2007 also indicate that the magnitude of the ATC proxy series from the TP is representative of the temperature difference between the mean temperature of June-August and that of the previous December-February. Although large tree-ring-based summer temperature reconstructions have been performed for high-latitude North America, there is no corresponding winter temperature reconstruction available. Therefore, an analysis of the summer-minus-winter temperature difference in this region is not currently feasible. The magnitudes of the ATC in North America (NA), northeastern Asia (NEA), the northern mid-latitudes (NHM), the northern high-latitudes (NHH) and the northern mid-high latitudes (NH) are calculated to be the gridded regional average of the CRUTEM4.6 land surface air temperature difference between the mean temperature of June-August and that of the previous December-February over the period 1851-2005. For definitions of the seven geographical regions used in this study, please see Supplementary Table 2. The following approaches were applied in each grid box and to all the regions analysed (Supplementary Figure 2, Supplementary Table 2) to calculate the summer-minus-winter temperature difference and to treat the missing data. The summer-minus-winter temperature difference was calculated for each grid box for every year based on the criterion that at least one month of data was available for both summer and winter; otherwise, the year was treated as having missing data. For the summer-minus-winter temperature difference series calculated in each grid box, only time series with at least 52 years of data (i.e., one-third of the length of the full period of 1851-2005) were defined as valid grid boxes and were used for further analysis. The percentage of valid grid boxes for each region analysed in this study is shown in Supplementary Table 2. Moreover, the grid boxes were used for trend analyses; for example, Figs.1a, c and e have data lengths of at least 52 consecutive years. The series of the regional magnitude of the ATC was produced by averaging all valid grid boxes in the corresponding regions (Supplementary Figure 2, Supplementary Table 2). Because the numbers of available valid grid boxes decreases for the regional series in the early time period, we test the influence of this decrease in the number of grid boxes on both the long-term trend and the non-overlapping 10-year-averaged series used for the D&A analyses (Supplementary Figures. 7-11). The results show that although the series of changes in the magnitude of ATC (with data coverage reduced to a minimum) can trigger changes in variance, little change occurred in the trend of the full-period and the non-overlapping 10-year-averaged series, both in the data rich period and in the full period. These results demonstrate that the decrease in number of valid grid boxes in the early period has little influence on the long-term trend of the magnitudes of the ATC and the D&A analyses conducted in this study. Atmospheric sulphate concentrations recorded in the TP ice core[17] and five Greenland ice cores (i.e., D20, GISP2, B16, B18 and B21; detailed in reference 29)[29] are used to indicate the sulphate emission strength caused by human activity.

**Change-point analysis.** We identified the change points in the trend of the reconstructed magnitude of the ATC in Europe and the TP using the SiZer (SIgnificant ZERo crossings of derivatives) method[30]. SiZer determines the change point and the significance of trends in time series data by performing an analysis across different smoothing bandwidths. For the bandwidths, the range of 15-50 years was considered suitable to reduce the influence of interannual to decadal climate variability on the detection of a sustained trend[15,30]. Therefore, we assess the change points of the magnitude of the ATC from the SiZer output by determining the median year of initiation for the most recent significant ($P < 0.1$) and sustained trends across the bandwidth range (in integer years from 15 to 50). The adaptability and stability of the SiZer method in addressing the climate changes that characterized industrial-era climate trends have been tested in reference 15, and a detailed description of the SiZer method is available in references 30 and 15. The code for performing the change-point analysis in this study is derived from reference 15.

**Model simulations.** Monthly mean land near-surface temperature (tas) simulations from 45 fully-coupled Earth system models (ESMs) participating in the CMIP5 project[20] (Supplementary Table 1) are used to perform the D&A analyses on the magnitude of the ATC over a long period. The ESMs comprise a set of simulations: ALL, with historical anthropogenic and natural forcings (i.e., solar variability; volcanic aerosols; well-mixed greenhouse gases; other anthropogenic factors, such as aerosols, land use/land cover change and/or ozone); GHG, with greenhouse gases forcing only (anthropogenic well-mixed greenhouse gases); NAT, with natural forcings only (solar variability and volcanic aerosols); ANT, with well-mixed greenhouse gases plus other anthropogenic factors (such as aerosols, land use/land cover change and/or ozone); AA, with anthropogenic aerosol forcings dominated by sulphate aerosols[24,25]; and internal climate variability (i.e., preindustrial control simulations, PiControl). Supplementary Table 1 shows the number of simulations runs used for each external forcing (i.e., ALL, NAT, ANT, GHG and AA) and model. Because climate models might overestimate the indirect effect of aerosol cooling[31], an alternative estimate of AA forcing was calculated as AA=ALL-NAT-GHG. Most of the external forcing simulations end in 2005. Monthly anomalies of the external forcing simulations are calculated for each grid box point and simulations based on the base period of 1961–1990. The PiControl simulations are treated as a time series, with an ending year of 2005, and monthly anomalies are calculated in the same way as the external forcing simulations. The anomalies are then re-gridded to a common grid of 5° × 5° and are masked to the corresponding range (Supplementary Table 2) to obtain the regionally averaged series. The multi-model ensemble means of the external forcing simulations are obtained by first computing the individual model ensemble mean and then averaging across all available models. This calculation gives equal weights to the different models and thus avoids models with larger numbers of ensemble members dominating the statistics of the multi-model mean.

**Detection and attribution (D&A) analysis.** Beyond the standard comparison of time series and trend patterns, one formal optimal fingerprint method[32,33] was applied to detect and attribute changes in the observed/reconstructed magnitude of the ATC in seven geographical areas (Supplementary Table 2, Supplementary Figure 12) since the late 19th century. The optimal fingerprint method is based on the generalized linear regression of the observed or reconstructed magnitude of the ATC as a combination of climate responses to external forcing plus internal variability. To detect and attribute the changes in the magnitude of the ATC (i.e., $ATC_{OBS}$) to different external forcings (i.e., $ATC_{ALL}$, $ATC_{ANT}$, $ATC_{NAT}$, $ATC_{GHG}$ and $ATC_{AA}$), we regressed the observed magnitude of the ATC onto different signal patterns under one-signal, two-signal and three-signal settings, respectively. The specific regression settings for the one-signal D&A analysis are as follows:

$ATC_{OBS} = \beta_{ALL} (ATC_{ALL} - \vartheta_{ALL}) + \varepsilon$ or $ATC_{OBS} = \beta_{ANT} (ATC_{ANT} - \vartheta_{ANT}) + \varepsilon$ or $ATC_{OBS} = \beta_{NAT} (ATC_{NAT} - \vartheta_{NAT}) + \varepsilon$.

The specific regression settings for the two-signal D&A analysis are as follows:

$$ATC_{OBS} = \beta_{ANT} (ATC_{ANT} - \vartheta_{ANT}) + \beta_{NAT} (ATC_{NAT} - \vartheta_{NAT}) + \varepsilon$$

The specific regression settings for the three-signal analysis are as follows:

$$ATC_{OBS} = \beta_{NAT} (ATC_{NAT} - \vartheta_{NAT}) + \beta_{GHG} (ATC_{GHG} - \vartheta_{GHG}) + \beta_{AA} (ATC_{AA} - \vartheta_{AA}) + \varepsilon.$$

where $ATC_{OBS}$ represents a vector of the observational or reconstructed magnitude of the ATC. $ATC_{ALL}$, $ATC_{ANT}$, $ATC_{NAT}$, $ATC_{GHG}$ and $ATC_{AA}$ (i.e., signal patterns) are calculated using the mean of a large ensemble of simulations from all available model simulations (Supplementary Figure 1). $\vartheta_{ALL}$, $\vartheta_{NAT}$, $\vartheta_{ANT}$, $\vartheta_{GHG}$ and $\vartheta_{AA}$ represent noise from internal variability in the corresponding signal patterns; $\beta_{ALL}$, $\beta_{NAT}$, $\beta_{ANT}$, $\beta_{GHG}$ and $\beta_{AA}$ represent the corresponding scaling factors; and ε represents the regression residual. The scaling factor and its uncertainty were estimated using the total least squares method[32,33]. The covariance structure of the noise terms is estimated from a long-term control simulation of the unforced climate (i.e., PiControl) with the model used in each analysis, and the estimates of the intra-ensemble variability are computed with the same model. The consistency of the unexplained signal (i.e., ε, which represents the residual of the regression) with internal variability was also assessed using a residual consistency test (RCT). The RCT implementation uses a non-parametric estimation of the null distribution through Monte Carlo simulations (see reference 32 for details).

The observational vector, ATC, which describes the space-time evolution of the ATC, is calculated with consecutive 10-year mean magnitude of the ATC over the analysis period for all seven regions. The purpose of 10-year averages is to suppress natural variability, particularly at interannual timescales[32,33]. According to the results of the change-point analyses of the reconstructed magnitude of the ATC in Europe and the TP (arrows in Fig. 2a, b) and the end year of the model simulations (2005), the periods 1865-2004 for Europe and 1872-2005 for the TP can be used for the long-term D&A

analysis. The European ATC proxy series ends in 2005[18]. Because there is not long enough ATC proxy evidence available to identify the year in which the sustained and significant ATC weakening began for northeastern Asia (NEA), North America (NA), the northern mid-latitudes (NHM), the northern high-latitudes (NHH) and the northern mid-high latitudes (NH), the earlier year identified in the proxies in Europe and the TP (i.e., 1865) is used as the beginning year of the ATC weakening for these regions. Thus, the available D&A analysis period for these five regions (i.e., NEA, NA, NHM, NHH and NH) can be from 1865 to 2004. Considering that as long as possible periods are used for dimension reduction (i.e., consecutive 10-year mean), the final selected period for the D&A analysis for the TP is 1872-2001 (13×10 yr) and for the other six regions is 1865-2004 (14×10 yr). Correspondingly, the PiControl simulations are divided into multiple non-overlapping 130-yr segments for the TP and 140-yr segments for the other six regions, with the last segments discarded if they are shorter than 130 years or 140 years (Supplementary Table 1). The one-signal and two-signal D&A analyses were conducted in all seven regions (Supplementary Table 2, Supplementary Figure 12), while the three-signal D&A analysis was conducted in three regions (i.e., NHM, NHH and NH) based on the latitude-dependent effects of GHGs and AAs on the change of the magnitude of the ATC identified in Fig. 3. All of the D&A analyses were performed using the code provided in reference 32.

**Data availability.** The data that support the findings of this study are available from the corresponding author upon request.

## References


1. IPCC 2013. Climate Change 2013: *The Physical Science Basis. Contribution of Working Group I to the Fifth Assessment Report of the Intergovernmental Panel on Climate Change* [Stocker, T.F., D. Qin, G.-K. Plattner, M. Tignor, S.K. Allen, J. Boschung, A. Nauels, Y. Xia, V. Bex and P.M. Midgley (eds.)]. Cambridge University Press, Cambridge, United Kingdom and New York, NY, USA, 1535 pp. (2013).
2. Stott, P. Attribution: Weather risks in a warming world. *Nat Clim Change* **5**, 516-517 (2015).
3. Christidis, N., Stott, P. A., Brown, S., Hegerl, G. C. & Caesar, J. Detection of changes in temperature extremes during the second half of the 20th century. *Geophys Res Lett* **32** (2005).
4. Hughes, L. Biological consequences of global warming: is the signal already apparent? *Trends Ecol Evol* **15**, 56-61 (2000).
5. Fussmann, K. E., Schwarzmuller, F., Brose, U., Jousset, A. & Rall, B. C. Ecological stability in response to warming. *Nat Clim Change* **4**, 206-210 (2014).
6. Soh, W. K., Wright, I. J., Bacon, K. L., Lenz, T. I., Steinthorsdottir, M., Parnell, A. C., & McElwain, J. C. A New Paleo-Leaf Economic Proxy Reveals a Shift in Ecosystem Function in Response to Global Warming at the Onset of the Triassic Period. *Nat Plants* 3, 17104, (2017).
7. Wang, G. & Dillon, M. E. Recent geographic convergence in diurnal and annual temperature cycling flattens global thermal profiles. *Nat Clim Change* 4, 988-992,

(2014).

8. Stine, A. R., Huybers, P. & Fung, I. Y. Changes in the phase of the annual cycle of surface temperature. *Nature* **457**, 435-440, (2009)
9. Mann, M. E. & Park, J. Greenhouse warming and changes in the seasonal cycle of temperature: Model versus observations. *Geophys Res Lett* **23**, 1111-1114 (1996).
10. Wallace, C. J. & Osborn, T. J. Recent and future modulation of the annual cycle. *Climate Res* **22**, 1-11 (2002).
11. Walther, G. R. *et al.* Ecological responses to recent climate change. *Nature* **416**, 389-395 (2002).
12. Li, Y., Huang, Y., Bergelson, J., Nordborg, M. & Borevitz, J. O. Association mapping of local climate-sensitive quantitative trait loci in *Arabidopsis thaliana. Proc. Natl Acad. Sci. USA* **197**, 201007431 (2010)
13. Qian, C. & Zhang, X. B. Human Influences on Changes in the Temperature Seasonality in Mid- to High-Latitude Land Areas. *J Climate* **28**, 5908-5921, (2015).
14. Ruddiman, W. F. *et al.* Late Holocene climate: Natural or anthropogenic? *Rev Geophys* **54**, 93-118 (2016).
15. Abram, N. J. *et al.* Early onset of industrial-era warming across the oceans and continents. *Nature* **536**, 411-418 (2016).
16. Duan, J. *et al.* Weakening of annual temperature cycle over the Tibetan Plateau since the 1870s. *Nat. Commun*. **8,** 14008 doi: 10.1038/ncomms14008 (2017).
17. Duan, K. Q., Thompson, L. G., Yao, T., Davis, M. E. & Mosley-Thompson, E. A 1000 year history of atmospheric sulfate concentrations in southern Asia as

recorded by a Himalayan ice core. *Geophys Res Lett* **34**, (2007).

18. Luterbacher, J., Dietrich, D., Xoplaki, E., Grosjean, M. & Wanner, H. European seasonal and annual temperature variability, trends, and extremes since 1500. *Science* **303**, 1499-1503, doi:DOI 10.1126/science.1093877 (2004).
19. Jones, P. D. *et al.* Hemispheric and large-scale land-surface air temperature variations: An extensive revision and an update to 2010. *J Geophys Res-Atmos* **117**, D05127 (2012).
20. Taylor, K. E., Stouffer, R. J. and Meehl, G. A. An overview of CMIP5 and the experiment design. *Bull. Amer. Meteor. Soc*. **93,** 485–498 (2012).
21. Rangwala, I., Sinsky, E. & Miller, J. R. Amplified warming projections for high altitude regions of the northern hemisphere mid-latitudes from CMIP5 models. *Environ Res Lett* **8** (2013).
22. Wang, H. J., Zeng, Q. C. & Zhang, X. H. The Numerical-simulation of the climatic-change caused by $CO_2$ doubling. *Sci China Ser B* **36**, 451-462 (1993).
23. Shindell, D. T., Miller, R. L., Schmidt, G. A. & Pandolfo, L. Simulation of recent northern winter climate trends by greenhouse-gas forcing. *Nature* **399**, 452-455 (1999).
24. Mitchell, J. F. B., Johns, T. C., Gregory, J. M. & Tett, S. F. B. Climate response to increasing levels of greenhouse gases and sulfate aerosols. *Nature* **376,** 501-504 (1995).
25. Bindoff, N. L. *et al. in IPCC Climate Change 2013: The Physical Science Basis* (eds Stocker, T. F. et al.) 867-931 (Cambridge Univ. Press, 2013).

26. Smith, S. J. *et al.* Anthropogenic sulfur dioxide emissions: 1850-2005. *Atmos Chem Phys* **11**, 1101-1116 (2011).

27. Hunter, D. E., Schwartz, S. E., Wagener, R. & Benkovitz, C. M. Seasonal, latitudinal, and secular variations in temperature trend - evidence for influence of anthropogenic sulfate. *Geophys. Res. Lett.* **20,** 2455–2458 (1993).

28. Meinshausen, M. *et al.* Historical greenhouse gas concentrations for climate modelling (CMIP6). *Geosci Model Dev* **10**, 2057-2116 (2017).

29. Fischer, H., Wagenbach, D. & Kipfstuhl, J. Sulfate and nitrate firn concentrations on the Greenland ice sheet - 2. Temporal anthropogenic deposition changes. *J Geophys Res-Atmos* **103**, 21935-21942, (1998)

30. Hannig, J. & Marron, J. S. Advanced distribution theory for SiZer. *J. Am. Stat. Assoc.* **101,** 484–499 (2006).

31. Sato, Y. *et al.* Aerosol effects on cloud water amounts were successfully simulated by a global cloud-system resolving model. *Nat Commun* **9** (2018).

32. Ribes, A., Planton, S. & Terray, L. Application of regularised optimal fingerprinting to attribution. Part I: method, properties and idealised analysis. *Climate Dynamics* **41**, 2817-2836, (2013).

33. Allen, M. R. & Stott, P. A. Estimating signal amplitudes in optimal fingerprinting, part I: theory. *Climate Dynamics* **21**, 477-491, (2003).

## Additional information

Correspondence and requests for materials should be addressed to J.D.

## Competing interests

The authors declare no competing interests.

## Acknowledgements

This research was supported by the National Key R&D Program of China (2016YFA0600404), the National Natural Science Foundation of China (41875113 and 41471035). Peili Wu was supported by the UK-China Research & Innovation Partnership Fund through the Met Office Climate Science for Service Partnership (CSSP) China as part of the Newton Fund. Jürg Luterbacher is supported by the Belmont Forum and JPI-Climate, Collaborative Research Action "INTEGRATE, An integrated data-model study of interactions between tropical monsoons and extratropical climate variability and extremes". Andrew Schurer and Gabriele Hegerl were supported by the ERC-funded project TITAN (EC-320691) and NERC under the Belmont forum, grant PacMedy (NE/P006752/1). Jianping Duan acknowledges support from the Alexander von Humboldt Foundation. We are very grateful to Prof. Keqin Duan and Prof. Hubertus Fischer for making their ice-core sulphate concentrations data available. We thank Dr. Aurélien Ribes for comments on the early manuscript. We are very grateful to the three anonymous reviewers who provided invaluable comments and suggestions that helped to improve our manuscript.

## Author contributions

J.D. designed the study and performed the analyses with support from Z.M. L.L. P.W. L. J and X. E. J.D. drafted and revised the manuscript with input from P.W. J. L. S. A.

G. H. D. G. and X. E. Y.D and L.C improved the figures. All authors contributed interpreting the results and discussions.

## Figures

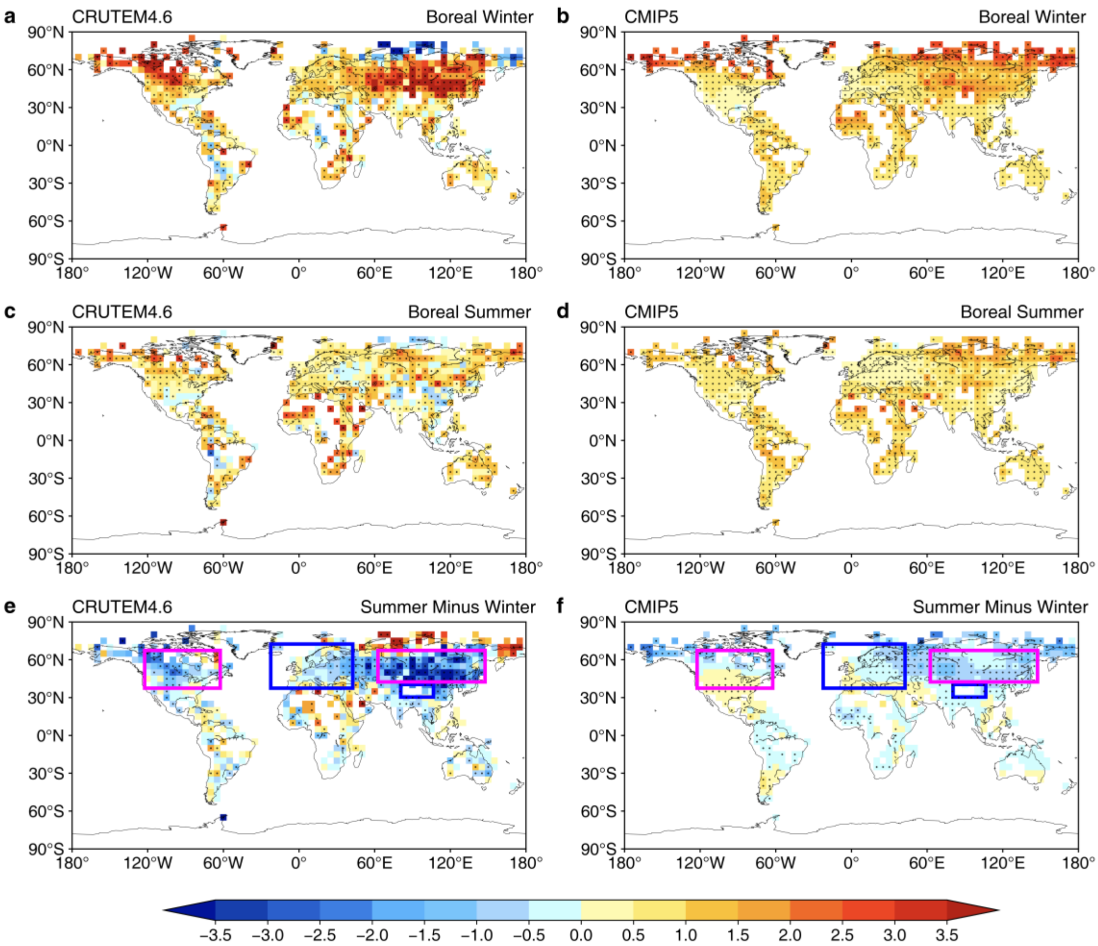


**Figure 1 | Linear trends (°C/100 yr) in the surface temperature seasonality for the period 1851-2005 calculated from observational records (CRUTEM4.6) (a, c, e) and the ensemble mean of the simulations from 45 ESMs driven by all forcings (b, d, f) for boreal winter (DJF) (a, b), boreal summer (JJA) (c, d) and the difference between summer and winter (e, f), with decreasing trends in the magnitude of the annual temperature cycle.** The black dots indicate a trend significance level of 0.05. The four boxes in (**e**) and (**f**) mark the regions of interest: the Tibetan Plateau, northeastern Asia, Europe and North America. Data derived from the ensemble mean of the simulations were masked to mimic the data availability of the CRUTEM4.6.

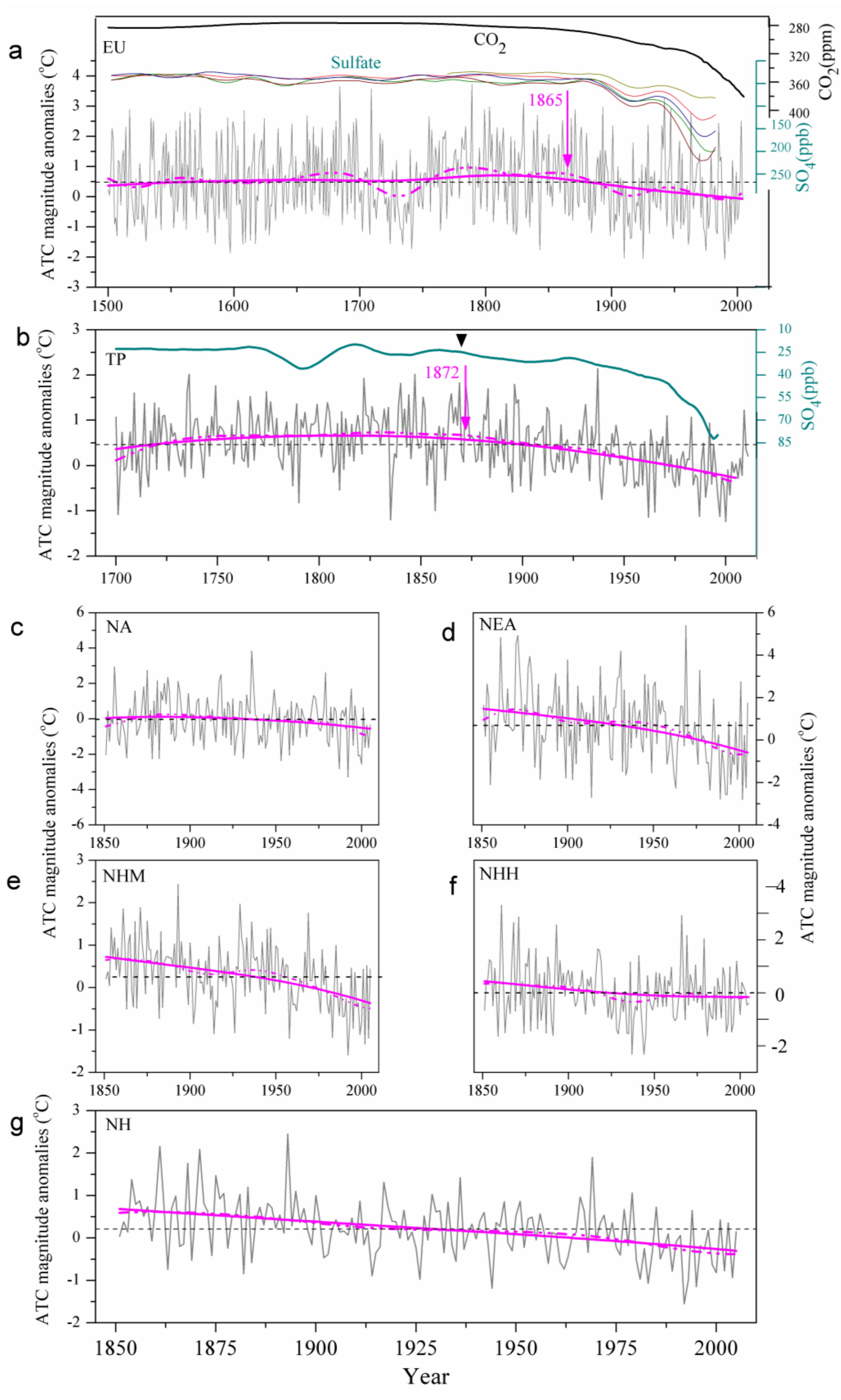


**Figure 2 | Time series of the magnitude of the regional annual temperature cycle (ATC) (grey) in comparison with $CO_2$ emissions (thick black line, increasing**

**downward) and sulphate concentrations recorded in ice cores (thin coloured lines, increasing downward) for (a) Europe (EU), with five Greenland ice cores over the period 1500-2004; (b) the Tibetan Plateau (TP), with one TP ice core over the period 1700-2011; and (c-g) North America (NA), northeastern Asia (NEA), the northern mid-latitudes (NHM), the northern high-latitudes (NHH) and the northern mid-high latitudes (NH) over 1865-2005.** The solid and dotted magenta lines represent 15-yr and 50-yr Gaussian smoothing of the magnitude of the ATC, respectively. The magenta arrow in (**a**) points to the year 1865, and that in (**b**) points to the year 1872. These arrows represent the median time of the onset of sustained, significant ATC weakening assessed across the 15-50-yr filter widths (Methods). The black triangle in (**b**) indicates the starting year (1870) of the human-induced sulphate concentration increase identified from the Dasuopu glacier located in the southern TP[17] and the dashed lines represent the mean magnitudes of the regional annual temperature cycle in the period. For the specific definition of the seven geographical regions used in this study, please see Supplementary Table 2.

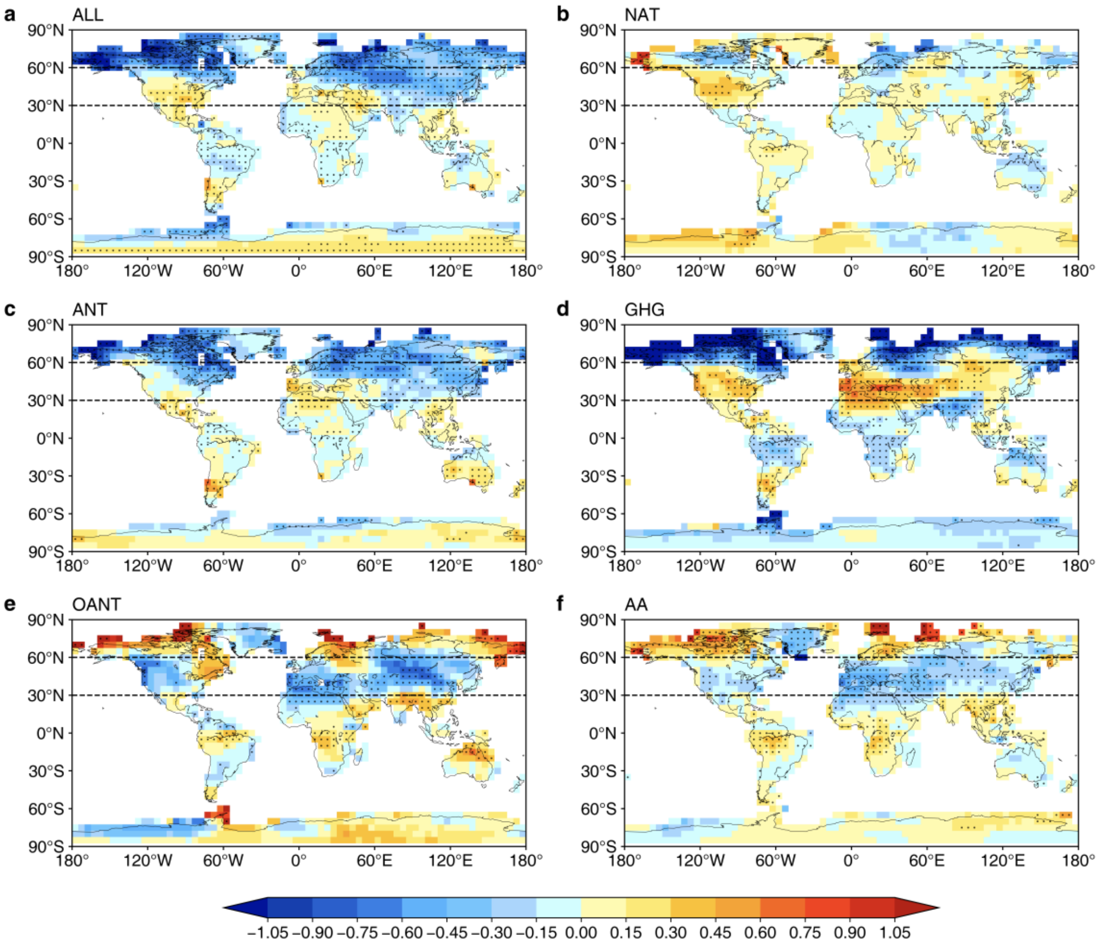


**Figure 3 | Linear treads (ºC/100 yr) in the simulated magnitude of the ATC over the period 1851-2005 driven by separate forcings for (a) ALL, (B) NAT, (c) ANT, (d) GHG, (e) OANT, (f) AA.** For the number of simulations and ESMs used for each forcing, please see supplementary Table 1. The black dots indicate a significance level of 0.05 for the trends. The black lines represent the 60°N and 30°N lines, respectively. The calculation for OANT is OANT=ALL-Nat-GHG, which stands for the other anthropogenic forcing derived mainly from anthropogenic aerosols (i.e., AA) but also from ozone and land use changes. The other forcings were calculated as the ensemble mean of multiple ESMs.

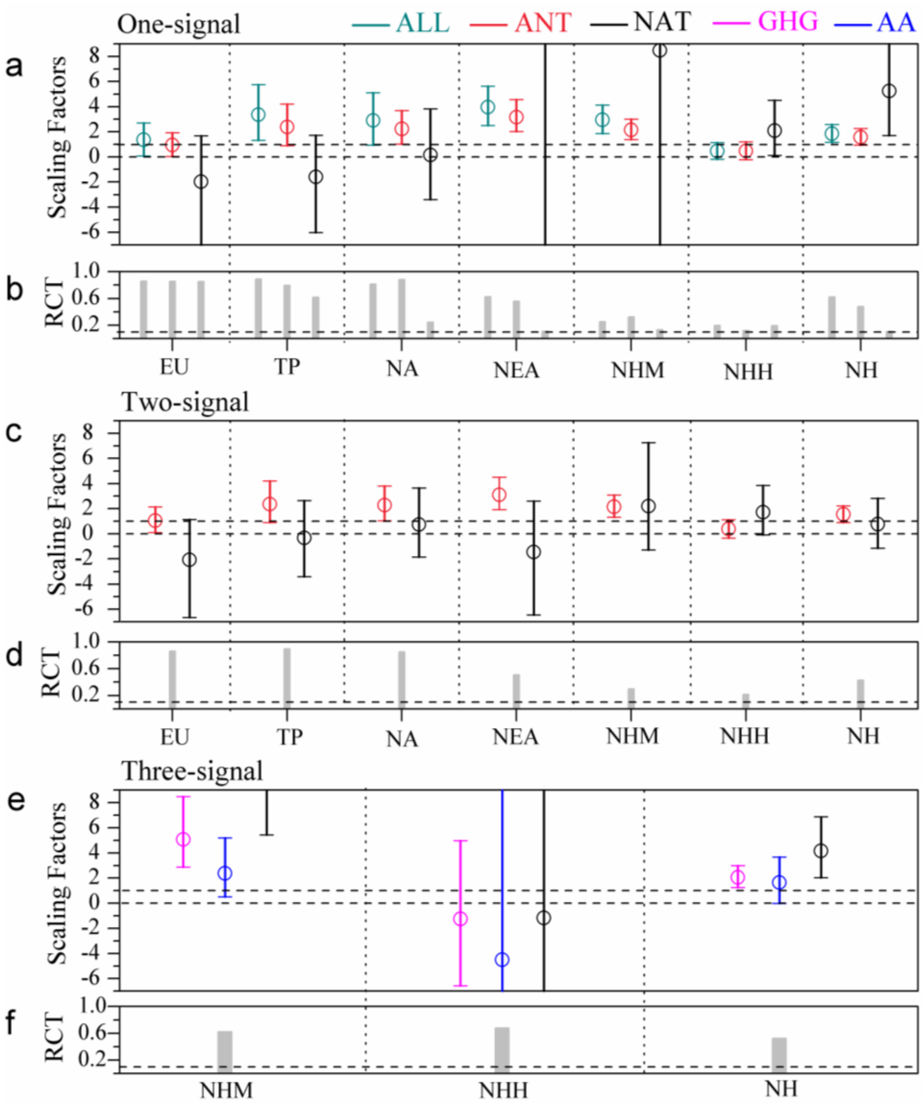


**Figure 4 | Results of the detection and attribution analyses applied to the magnitude of the ATC in seven regions.** Scaling factors and the residual consistency test (RCT) derived from the one-signal analysis (**a, b**), two-signal analysis (**c, d)** and three-signal analysis (**e, f**) (Methods). The confidence interval for the scaling factors is 90%. The analysis period for Europe (EU), North America (NA), northeastern Asia (NEA), the northern mid-latitudes (NHM), the northern high-latitudes (NHH) and the northern mid-high latitudes (NH) is from 1865-2004 and that for the Tibetan Plateau (TP) is from 1872-2001 (Methods).

## Supplementary Information

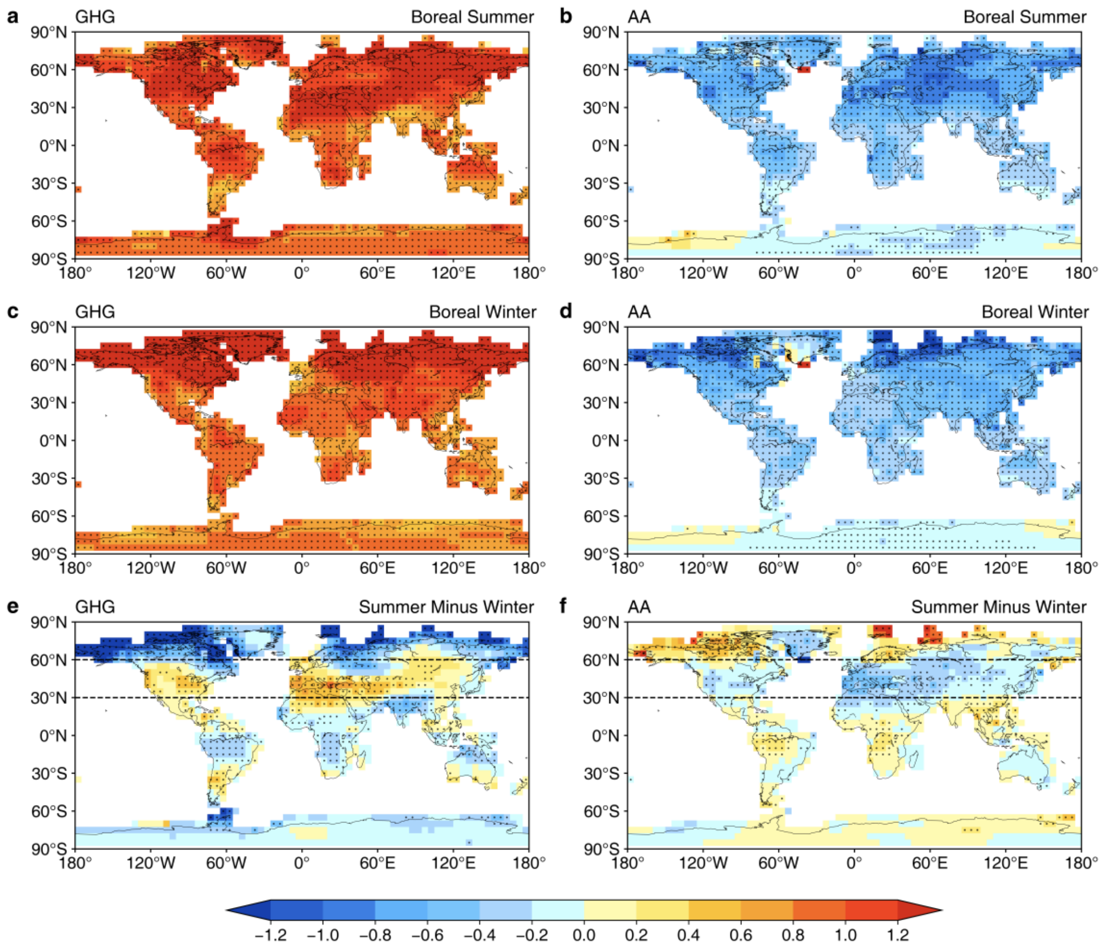


**Figure S1 | Linear trends (ºC/100 yr) in the surface temperature seasonality for the period 1851-2005 driven by GHGs (a, c, e) and AAs (b, d, f) for boreal summer (JJA) (a, b), boreal winter (DJF) (c, d) and the difference between summer and winter (e, f).** The black dots indicates a significance level of 0.05 for the trends. The dotted black lines represent the 60ºN and 30ºN lines. The GHGs and AAs were calculated as the ensemble mean of multiple GCMs (Supplementary Table 1).

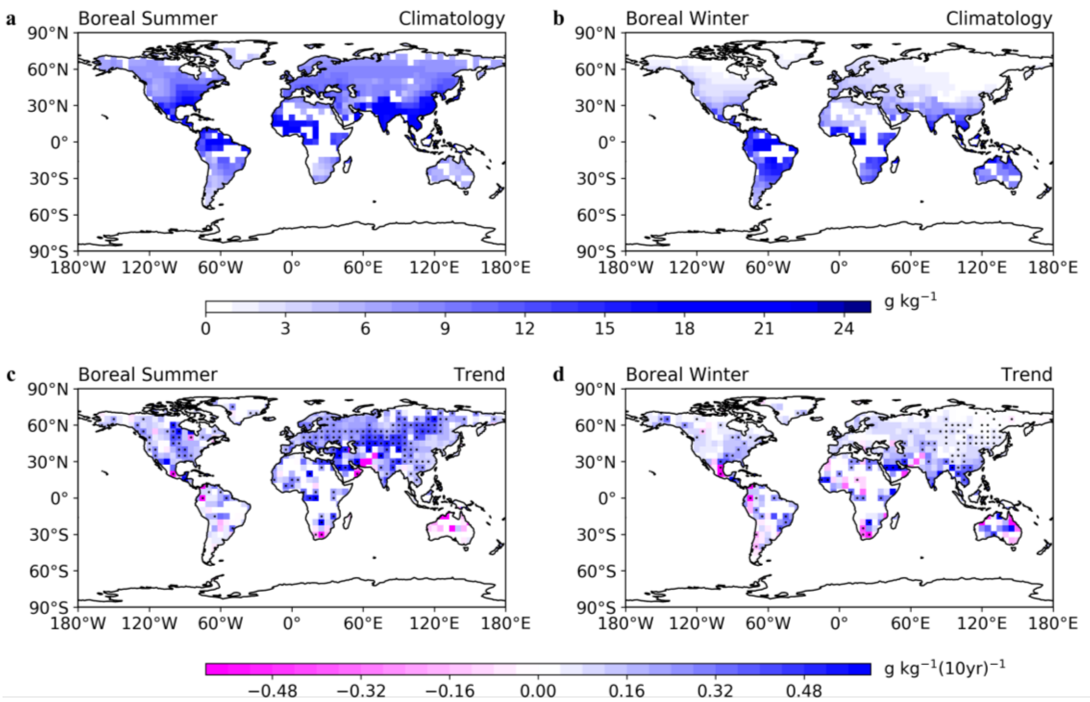


**Figure S2 | Spatial pattern and linear trend of the specific humidity in summer (JJA) and winter (DJF)**. Multi-year-averaged summer (a) and winter (b) specific humidity and the linear trend in summer (c) and winter (d) over the period 1973-2017.

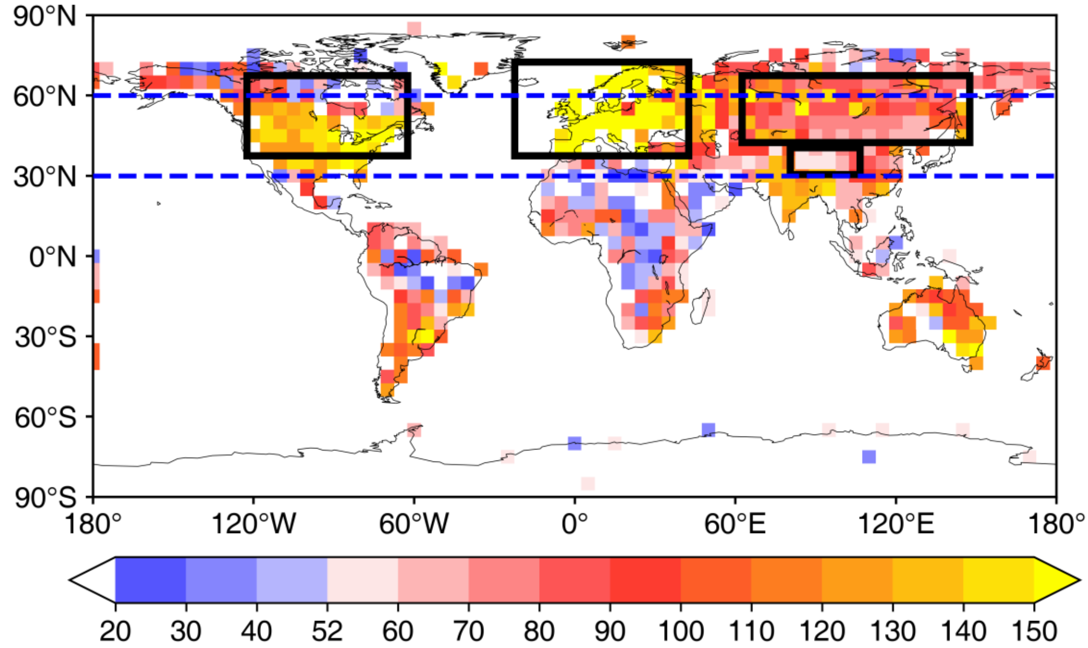


**Figure S3 | The amount of available data on the magnitude of the ATC (i.e., the summer-minus-winter temperature difference) from the CRUTEM4.6 dataset for each grid box over the period 1851-2005.** The four boxes mark the regions of interest (please also see Fig. 1) and the dotted blue lines represent the 30ºN and 60ºN lines.

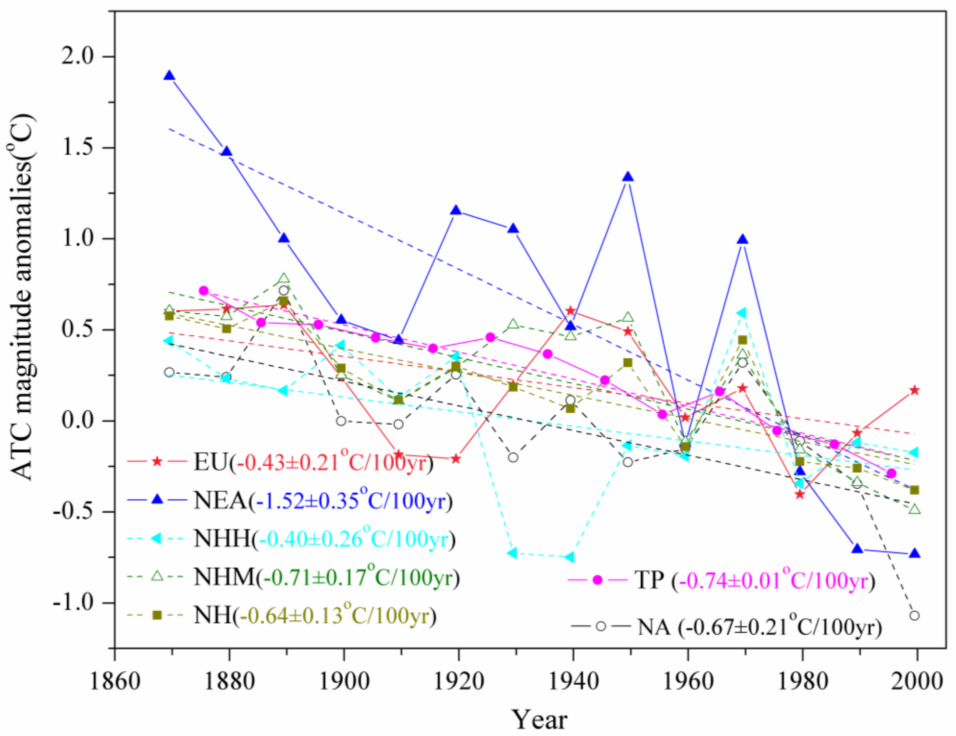


**Figure S4 | Trends of the observed/reconstructed magnitude of the ATC for seven regions over its period of weakening, as identified by the change-point analysis shown in Fig. 2.** The trends calculated for Europe (EU), northeastern Asia (NEA), North America (NA), the northern high-latitudes (NHH), the northern mid-latitudes (NHM) and the northern mid-high-latitudes (NH) are based on 10-year mean data over the period 1865-2004, and those for the TP are based on 10-year mean data over the period 1872-2001. Uncertainties in the trends include the reduction in the number of degrees of freedom due to serial correlation of the regression residuals.

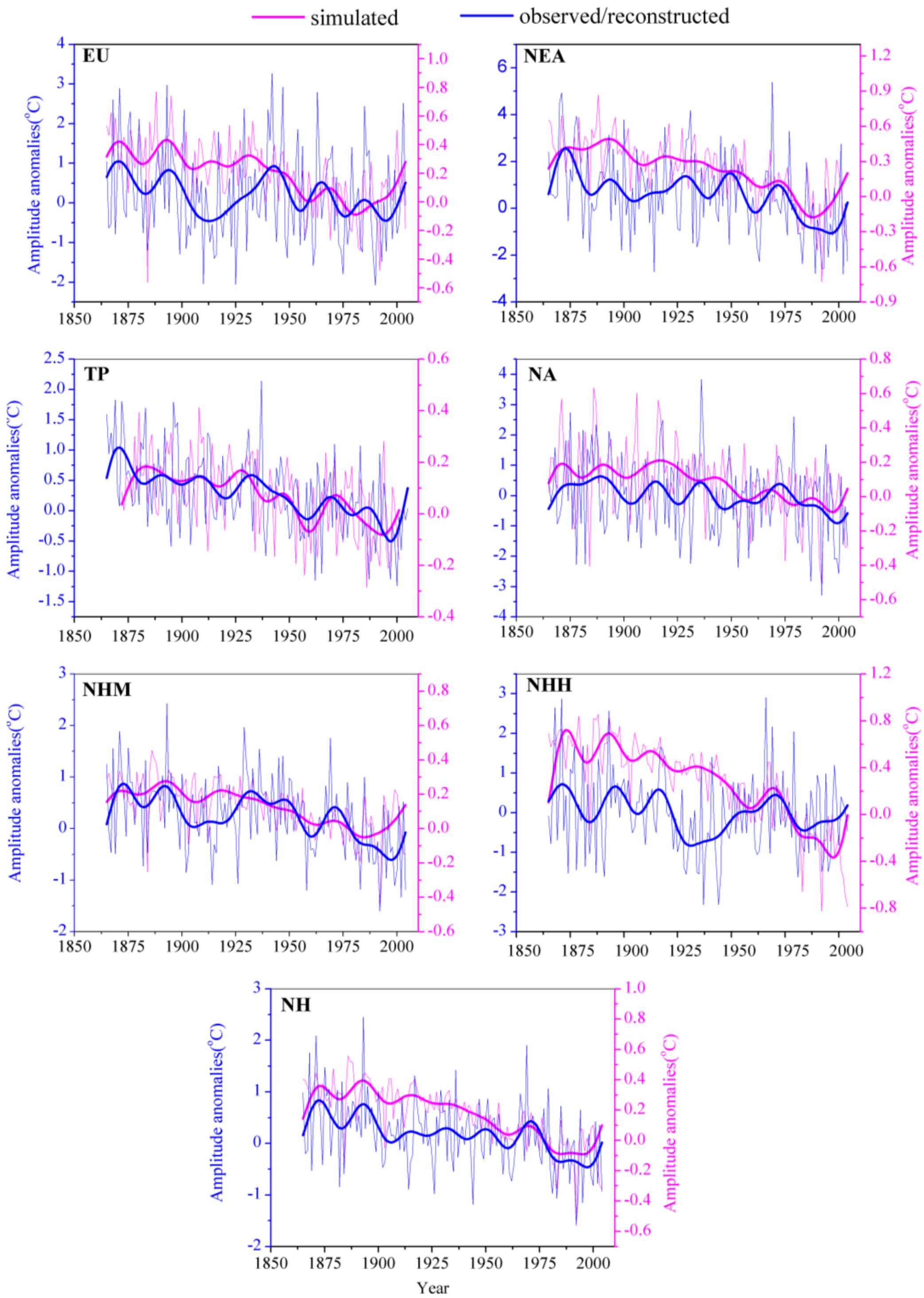


**Figure S5 | Comparisons between the simulated and observed/reconstructed magnitude of the ATC.** The thin lines represent annual values and the thick lines present the 11-year fast Fourier filter (FFT).

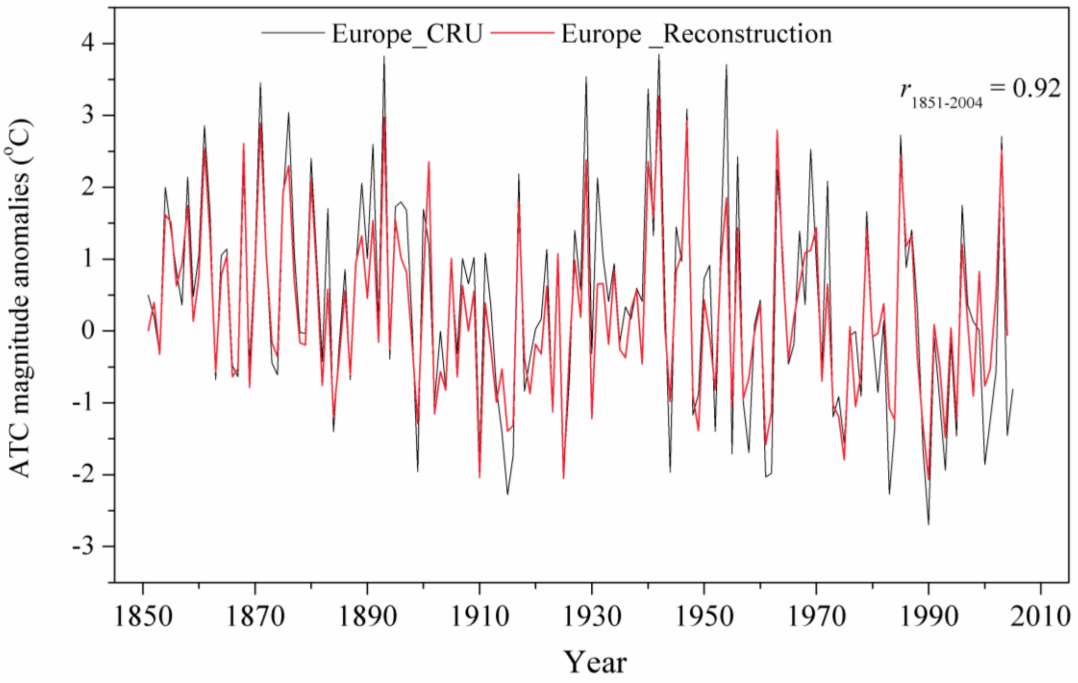


**Figure S6 | Comparison between the reconstructed and observed magnitude of the ATC for Europe.**

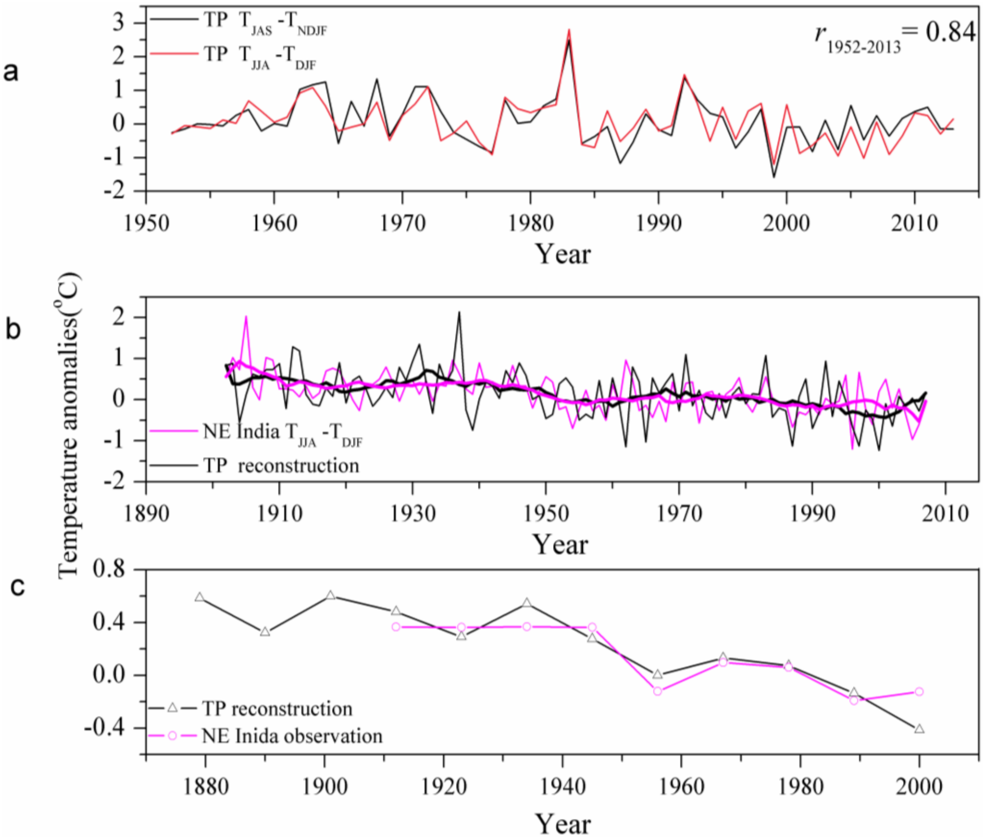


**Figure S7 | Comparisons between the reconstructed magnitudes of the ATC on the TP and the observational records derived from different seasons.** (**a**) Comparisons between the mean temperature of July-September minus that of the previous November to February and the mean temperature of June-August minus that of the previous December to February over the TP during 1952-2013. (**b**) Comparisons of the reconstructed magnitude of the ATC and the observational record (the mean temperature of June-August minus that of the previous December to February) over northeast India during the common period 1902-2007. (**c**) Same as in (**b**) but for the 11-year mean. Note that all temperature anomalies are with respect to the mean of 1961-1990 and the thick lines in (**b**) represent the 11-year moving average.

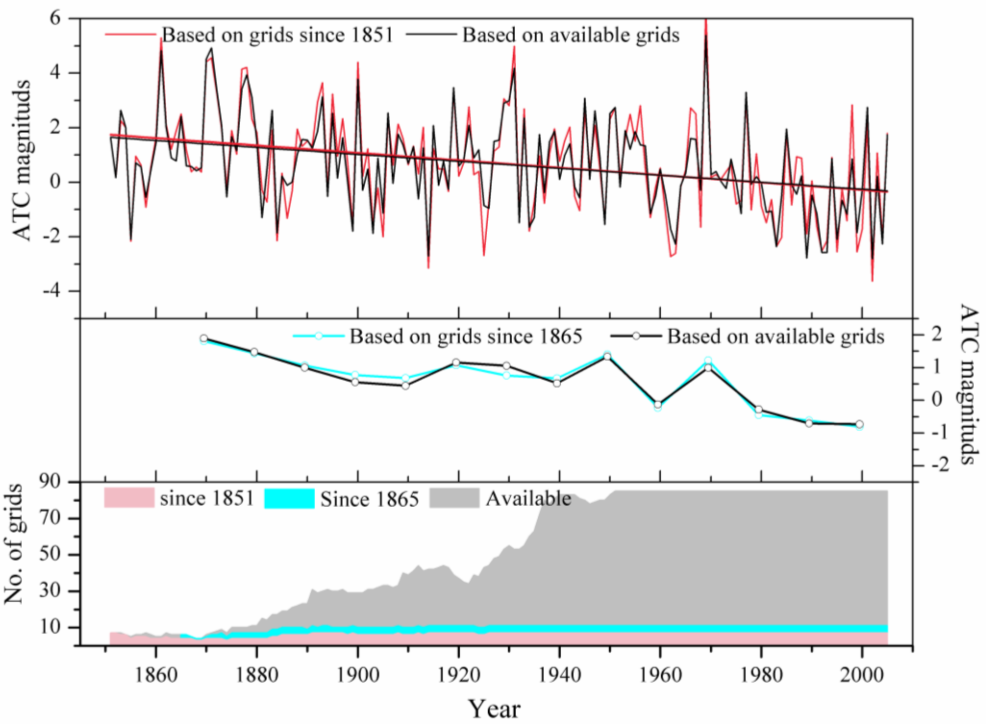


**Figure S8** Comparisons between the regional series of the magnitudes of the ATC in northeastern Asia (NEA) obtained by averaging the series from the available grid boxes (i.e., valid grid boxes, Supplementary Table 2) and the regional series of the magnitudes of the ATC in NEA produced using data coverage reduced to a minimum in the region. (a) Comparisons of the annual value and the full-period trend between the two regional series produced using different methods above; (b) comparisons of the non-overlapping 10-year mean between the two regional series produced using different methods above, which is used for the D&A analysis; (c) the amount of grid boxes used for producing the series in (a) and (b).

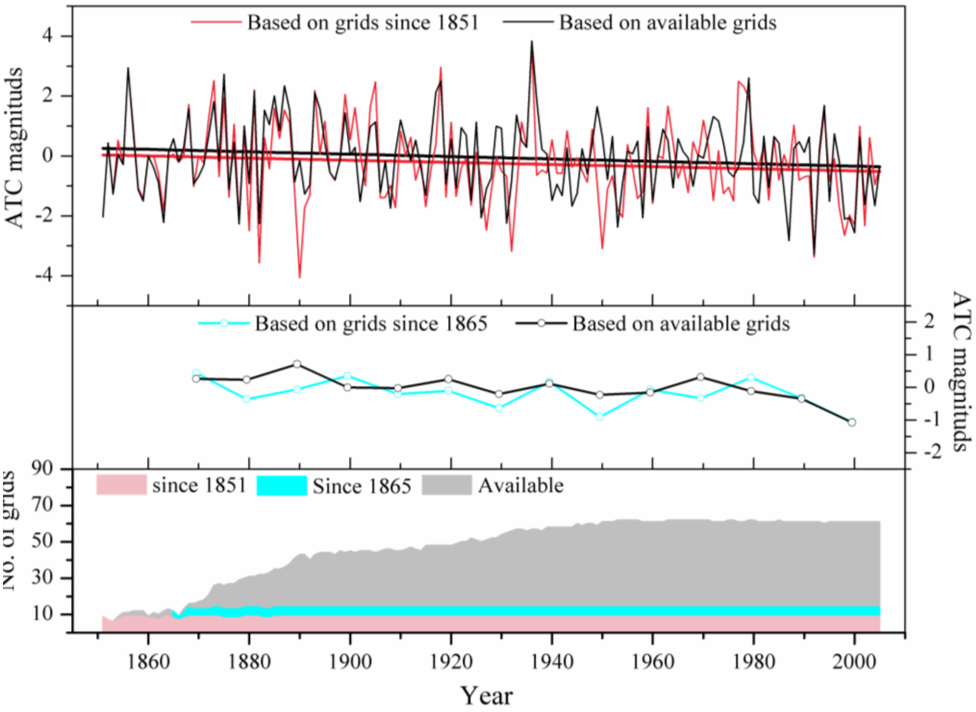


**Figure S9** Same as Fig. S8, but for North America

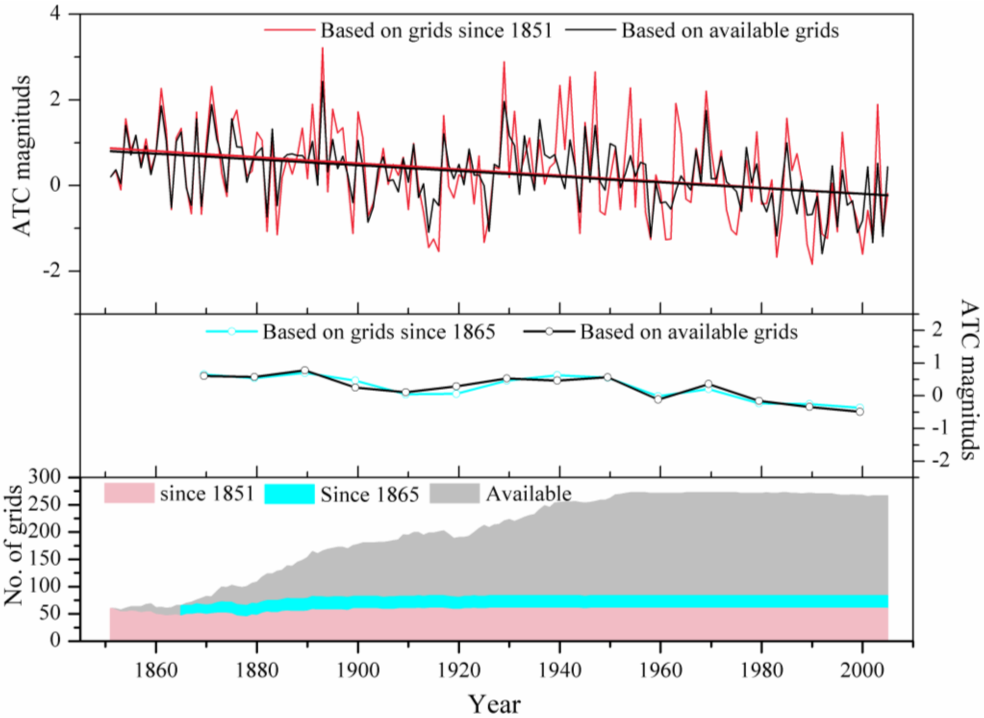


**Figure S10** Same as Fig. S8, but for the northern mid-latitudes.

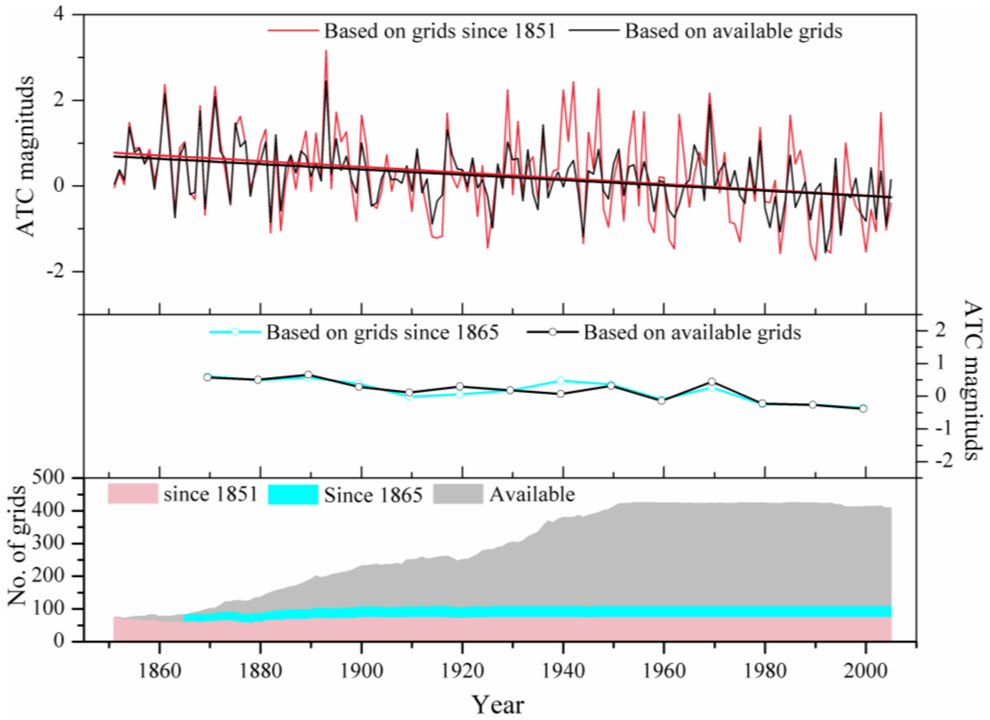


**Figure S11** Same as Fig. S8, but for the northern mid-high latitudes.

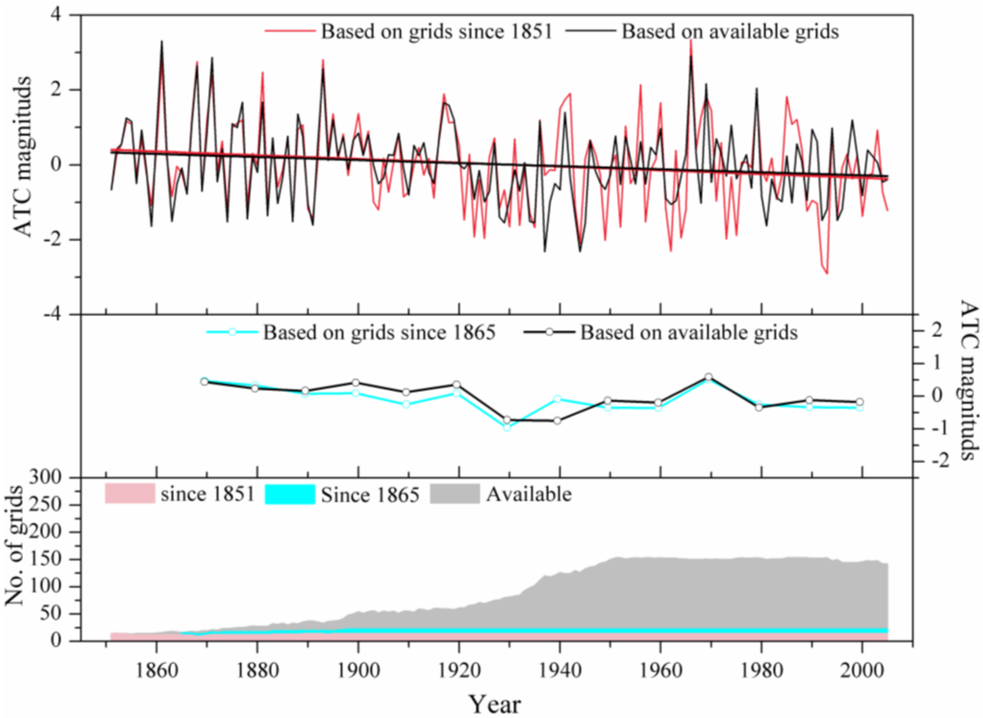


**Figure S12** Same as Fig. S8, but for the northern high-latitudes.

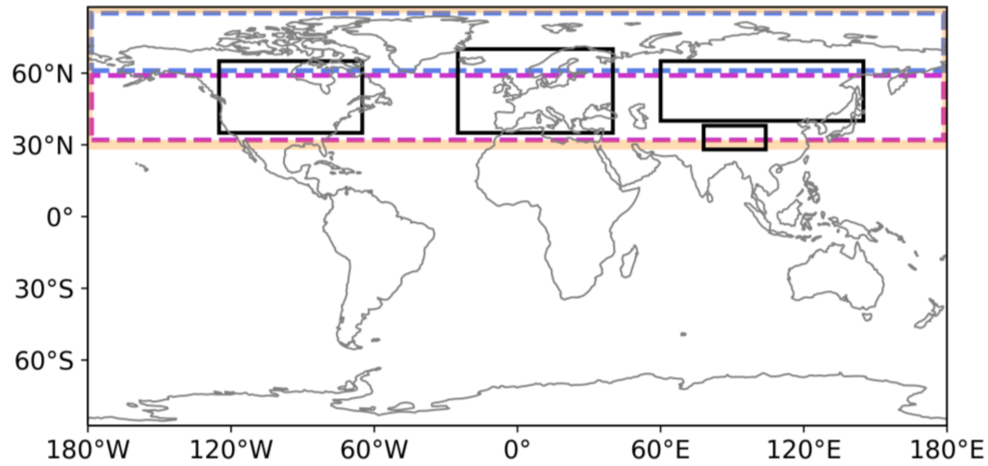


**Figure S13** A diagram showing the geographical areas chosen for the one-signal (all seven regions), two-signal (all seven regions) and three-signal (the three coloured boxes) detection and attribution analyses in Fig. 4. For specific information on the latitude and longitude, please see Supplementary Table 2.

**Table S1.** List of CMIP5 models, experiments and number of ensemble members for this study. The last row shows the number of models for each forcing.

| No. | Model | All | ANT | GHG | NAT | AA | PiC1 | PiC2 |
|---|---|---|---|---|---|---|---|---|
| M1 | ACCESS1-0 | 2 | | | | | 3 | 3 |
| M2 | ACCESS1-3 | 3 | | | | | 3 | 3 |
| M3 | BNU-ESM | 1 | | 1 | 1 | | 4 | 4 |
| M4 | CCSM4 | 8 | 4 | 3 | 4 | 3 | 9 | 8 |
| M5 | CESM1-BGC | 1 | | | | | 3 | 3 |
| M6 | CESM1-CAM5 | 3 | 3 | 1 | 3 | 3 | 2 | 2 |
| M7 | CESM1-FASTCHEM | 3 | | | | | 1 | 1 |
| M8 | CESM1-WACCM | 1 | | | | | 1 | 1 |
| M9 | CMCC-CESM | 1 | | | | | 2 | 2 |
| M10 | CMCC-CMS | 1 | | | | | 3 | 3 |
| M11 | CMCC-CM | 1 | | | | | 2 | 2 |
| M12 | CNRM-CM5-2 | 1 | | | | | 4 | 4 |
| M13 | CNRM-CM5 | 10 | 10 | 6 | 6 | | 6 | 6 |
| M14 | CSIRO-Mk3.6.0 | 10 | 5 | 5 | 5 | 5 | 3 | 3 |
| M15 | CanESM2 | 5 | | 5 | 5 | 5 | 7 | 7 |
| M16 | EC-EARTH | 5 | | | | | 3 | 3 |
| M17 | FGOALS-g2 | 5 | | 1 | 3 | 1 | 5 | 5 |
| M18 | FGOALS-s2 | 2 | | | | | 3 | 3 |
| M19 | FIO-ESM | 3 | | | | | 6 | 5 |
| M20 | GFDL-CM3 | 4 | 3 | 3 | 3 | 3 | 3 | 3 |
| M21 | GFDL-ESM2M | 1 | 1 | 1 | 1 | 1 | 3 | 3 |
| M22 | GISS-E2-H-CC | 1 | | | | | 1 | 1 |
| M23 | GISS-E2-H | 18 | 10 | 5 | 10 | | 9 | 7 |
| M24 | GISS-E2-H310 | | | | | 5 | | |

Continue the above page

| | | | | | | | | |
|---|---|---|---|---|---|---|---|---|
| M25 | GISS-E2-H107 | | | | | 5 | | |
| M26 | GISS-E2-R-CC | 1 | | | | | 1 | 1 |
| M27 | GISS-E2-R | 24 | 10 | 5 | 10 | | 23 | 20 |
| M28 | GISS-E2-R310 | | | | | 5 | | |
| M29 | GISS-E2-R107 | | | | | 5 | | |
| M30 | HadCM3 | 10 | | | | | | |
| M31 | HadGEM2-AO | 1 | | | | | 5 | 5 |
| M32 | HadGEM2-ES | 3 | | 4 | 4 | | | |
| M33 | IPSL-CM5A-LR | 6 | 3 | 5 | 3 | | 7 | 7 |
| M34 | IPSL-CM5A-MR | 3 | | 3 | 3 | 1 | 2 | 2 |
| M35 | IPSL-CM5B-LR | 1 | | | | | 2 | 2 |
| M36 | MIROC-ESM-CHEM | 1 | | 1 | 1 | | 2 | 1 |
| M37 | MIROC-ESM | 3 | | 3 | 3 | | 4 | 4 |
| M38 | MIROC5 | 5 | | | | | 5 | 4 |
| M39 | MPI-ESM-LR | 3 | | | | | 7 | 7 |
| M40 | MPI-ESM-MR | 3 | | | | | 7 | 7 |
| M41 | MPI-ESM-P | 2 | | | | | 8 | 8 |
| M42 | MRI-CGCM3 | 5 | | 1 | 1 | | 3 | 3 |
| M43 | NorESM1-ME | 2 | | | | | 1 | 1 |
| M44 | NorESM1-M | 3 | | 1 | 1 | 1 | 3 | 3 |
| M45 | bcc-csm1-1-m | 3 | | | | | 3 | 2 |
| M46 | bcc-csm1-1 | 3 | | 1 | 1 | | 3 | 3 |
| M47 | Inmcm4 | 1 | | | | | 3 | 3 |
| M48 | HadGEM2-CC | | | | | | 1 | 1 |
| | Sum(models) | 173(43) | 49(9) | 55(19) | 68(19) | 43(13) | 177(42) | 166(42) |

Note: piC1 and piC2 indicate PiControl for the Tibetan Plateau and the other six regions (Supplementary Table 2), respectively.

**Table S2.** Definition of the seven geographical areas used for the detection and attribution analyses in this study.

| *Geographical areas* | Tibetan Plateau | Europe | North America | Northeastern Asia | Northern mid-latitudes | Northern high-latitudes | Northern mid- to high-latitudes |
|---|---|---|---|---|---|---|---|
| *Abbreviation* | TP | EU | NA | NEA | NHM | NHH | NH |
| *Latitudes and longitudes* | 78°-104°E, 28°-38°N. | -25°-40°E, 35°-70°N | 65°-125°W, 35°-65°N | 60°-145°E, 40°-65°N | 30°-60°N, -180°-180°E | 60°-87.5°N, -180°-180°E | 30°-87.5°N, -180°-180°E |
| *No. of valid grid box* | proxy | proxy | 86% | 100% | 63% | 49% | 35% |

*No. of valid grid box* indicates the percent of grid boxes with available data for more than 52 years over the period 1851-2005 (i.e., one-third length of the full period). The "proxy" indicates the D&A analysis was based on a proxy series.